

Photoelectron imaging of modal interference in plasmonic whispering gallery cavities

Pascal Melchior,¹ Deirdre Kilbane,¹ Ernst Jan Vesseur,² Albert Polman,²
and Martin Aeschlimann^{1,*}

¹Physics Department and Research Center OPTIMAS, University of Kaiserslautern, Erwin-Schrödinger-Str. 46,
67663 Kaiserslautern, Germany

²FOM Institute AMOLF, Science Park 104, 1098 XG Amsterdam, The Netherlands

*ma@physik.uni-kl.de

Abstract: We use three-photon photoemission electron microscopy (PEEM) to investigate the interference of coherently excited dipolar and quadrupolar resonant modes of plasmonic whispering gallery resonators formed by circular grooves patterned into a flat Au surface. Optical scattering and cathodoluminescence spectroscopy are used to characterize the cavity resonance spectra for a wide range of cavity radii and groove depths. Using PEEM, we directly resolve the interference between the modal field distribution of dipolar and quadrupolar modes that are coherently excited at $\lambda = 795$ nm under oblique incidence. Characteristic asymmetries in the photoelectron images for both TM and TE excitation are a direct consequence of the coherent excitation of the resonant modes.

©2015 Optical Society of America

OCIS codes: (250.5403) Plasmonics; (240.6680) Surface plasmons; (320.7080) Ultrafast devices; (240.6675) Surface photoemission and photoelectron spectroscopy; (250.1500) Cathodoluminescence; (100.0118) Imaging ultrafast phenomena.

References and links

1. F. Vollmer and S. Arnold, "Whispering-gallery-mode biosensing: label-free detection down to single molecules," *Nat. Methods* **5**(7), 591–596 (2008).
 2. S. I. Bozhevolnyi, V. S. Volkov, E. Devaux, and T. W. Ebbesen, "Channel plasmon-polariton guiding by subwavelength metal grooves," *Phys. Rev. Lett.* **95**(4), 046802 (2005).
 3. E. J. R. Vesseur, F. J. García de Abajo, and A. Polman, "Modal decomposition of surface-plasmon whispering gallery resonators," *Nano Lett.* **9**(9), 3147–3150 (2009).
 4. E. J. R. Vesseur, F. J. García de Abajo, and A. Polman, "Broadband Purcell enhancement in plasmonic ring cavities," *Phys. Rev. B* **82**(16), 165419 (2010).
 5. S. I. Bozhevolnyi, V. S. Volkov, E. Devaux, and T. W. Ebbesen, "Channel plasmon-polariton guiding by subwavelength metal grooves," *Phys. Rev. Lett.* **95**(4), 046802 (2005).
 6. E. J. R. Vesseur and A. Polman, "Plasmonic whispering gallery cavities as optical nanoantennas," *Nano Lett.* **11**(12), 5524–5530 (2011).
 7. P. Kahl, S. Wall, C. Witt, C. Schneider, D. Bayer, A. Fischer, P. Melchior, M. Horn-von Hoegen, M. Aeschlimann, and F.-J. Meyer zu Heringdorf, "Normal-incidence photoemission electron microscopy (NI-PEEM) for imaging surface plasmon polaritons," *Plasmonics* **9**(6), 1401–1407 (2014).
 8. P. A. Anderson, "Work function of gold," *Phys. Rev.* **115**(3), 553–554 (1959).
 9. H. B. Michaelson, "The work function of the elements and its periodicity," *J. Appl. Phys.* **48**(11), 4729–4733 (1977).
 10. M. V. Bashevov, F. Jonsson, A. V. Krasavin, N. I. Zheludev, Y. Chen, and M. I. Stockman, "Generation of traveling surface plasmon waves by free-electron impact," *Nano Lett.* **6**(6), 1113–1115 (2006).
 11. W. Cai, R. Sainidou, J. Xu, A. Polman, and F. J. García de Abajo, "Efficient generation of propagating plasmons by electron beams," *Nano Lett.* **9**(3), 1176–1181 (2009).
 12. E. J. R. Vesseur, R. de Waele, M. Kuttge, and A. Polman, "Direct observation of plasmonic modes in au nanowires using high-resolution cathodoluminescence spectroscopy," *Nano Lett.* **7**(9), 2843–2846 (2007).
 13. T. Coenen, F. Bernal Arango, A. Femius Koenderink, and A. Polman, "Directional emission from a single plasmonic scatterer," *Nat. Commun.* **5**, 3250 (2014).
 14. R. C. Word, J. P. S. Fitzgerald, and R. Könenkamp, "Positional control of plasmonic fields and electron emission," *Appl. Phys. Lett.* **105**(11), 111114 (2014).
-

1. Introduction

As nano-optical devices promise a large variety of applications and interesting questions for fundamental research, the investigation of plasmonic excitations in nanostructures has evolved into a very active research field. Plasmonic whispering gallery mode (WGM) cavities are highly interesting for their use as biosensors for the label-free detection of biomolecules with a sensitivity down to a single-molecule level [1]. The attractiveness of these structures lies in the strong field enhancement inside these cavities and their miniature device dimensions. Plasmonic WGM cavities consist of a circular groove that is carved into a planar gold surface [Fig. 1(a)]. The groove sustains bound surface plasmon polaritons (SPPs) that are confined between the two closely spaced groove sidewalls [Fig. 1(b)] [2,3]. The resulting resonator eigenmodes result from circulating plasmons that form a standing wave pattern along the ring circumference.

The lowest-order azimuthal resonance $m = 1$ in these plasmonic whispering gallery cavities occurs if the ring circumference equals a single plasmon wavelength λ_p . The corresponding standing wave modal field distribution then has a dipolar charge distribution. As the ring diameter increases, the plasmonic WGM cavities support azimuthal modes of higher order, corresponding to quadrupolar and higher-order field distributions [3]. Furthermore, rings with deep grooves show higher-order radial modes with order $n = 0, 1, 2, \dots$ that correspond to the number of antinodes of the near-field in the radial direction and the groove of the cavity. Through the independent control of azimuthal and radial mode symmetry these WGM cavities provide unique control over the local resonance spectrum and the near-to-far-field coupling. In [3–5] a dispersion model that relates circular grooves to straight grooves explains the dependence of mode frequencies and spatial distributions on ring radius and groove depth. Resonant circulating groove plasmons satisfy the relation $k_z = m/R$, where k_z is the wave vector of the straight-groove plasmon, m is the azimuthal order and R is the ring radius. Additionally, deep grooves confine modes with wave vector larger than the SPP wave vector for a planar gold surface with a localization that grows with increasing groove depth. This results in CL emission resonance peaks that shift to longer wavelength for increasing radius and depth. In addition the resonance wavelength depends critically on the groove width and the radius of the tip of the groove. The strong sensitivity to geometry can make the resonances very sensitive to the adhesion of *e. g.* biomolecules in the WGR.

Previously, far-field methods like confocal microscopy or dark field scattering microscopy have been used to determine the spectral properties of plasmonic antennas. However, the spectral features and near-field properties of resonant WGM cavities are determined on a length scale that is much smaller than the spatial resolution of these purely optical methods. Therefore, high-resolution spatial imaging of the plasmonic modal field distribution and resonance spectra is essential to obtain full understanding of the underlying mechanisms that lead to the observed near-field enhancement, interference, and mode hybridization.

In recent years, two complementary techniques have been introduced that enable optical imaging at a deep-subwavelength scale using a combination of photons and electrons: cathodoluminescence imaging spectroscopy (CL) and photoemission electron microscopy (PEEM). In CL, the material is excited with a high-energy electron beam (typically 30 keV) and the emitted light is collected. In contrast, PEEM uses optical excitation while the photoelectrons are collected. Recently, CL was used to determine the resonant spectra of plasmonic WGM cavities made in a Au surface as a function of cavity diameter, radius and groove depth [3,4,6]. So far however, the determination of the local near-field distributions has remained elusive, because CL delivers information about the far-field radiation pattern only and does not allow an unambiguous statement about the local interaction of different resonant modes [6]. Here, we use PEEM on the same samples first studied with CL, to directly determine the local near-field of the WGM cavities with great precision. We systematically study the spectral shifts of PEEM resonances with resonator width and depth, and determine the modal near-field distributions for both dipolar and quadrupolar resonances, as well as the consequence of their interaction.

2. Photoemission electron microscopy, cathodoluminescence and optical extinction spectroscopy of plasmonic ring resonators

Arrays of plasmonic WGM ring resonators were patterned into a smooth Au surface that was obtained by thermal evaporation of a 3- μm -thick Au layer onto a freshly cleaved mica substrate. After annealing at 500° C a silicon wafer is glued onto the Au layer, which is then stripped off the mica substrate. V-shaped grooves were then cut into the Au surface using focused-ion-beam milling using a 30 keV Ga beam. Grooves were approximately 100 nm wide at the top with a depth in the range $d = 60\text{--}140, 500$ nm and ring radius in the range $r = 100\text{--}300$ nm. Both the groove depth and the ring radius are varied systematically resulting in a 10×11 matrix of rings, as shown in the scanning electron micrograph in Fig. 1(c). The spacing between rings was large enough to avoid diffraction effects.

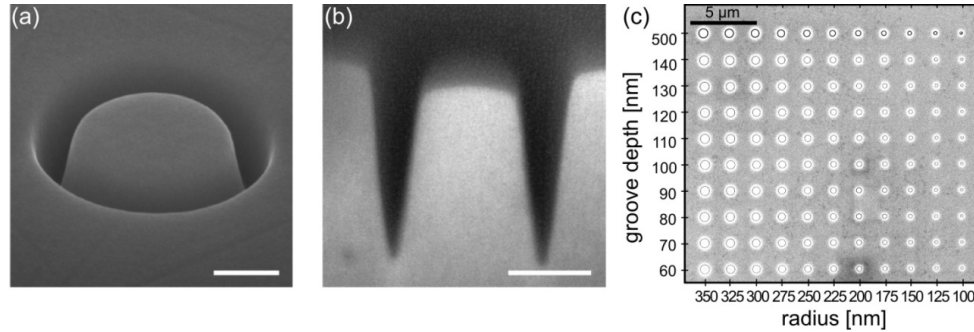


Fig. 1. (a) Scanning electron micrograph taken under an angle of 52° of a single ring resonator in Au made using template stripping. The ring is visible as a circular groove in the center with radius $r = 300$ nm. Scale bar: 200 nm. (b) FIB-milled cross section through a single ring resonator in Au. Scale bar: 200 nm. (c) Top-view SEM image of a 10×11 array of ring resonators with $r = 100\text{--}350$ nm and $d = 60\text{--}140, 500$ nm.

PEEM (NI-IS-PEEM, Focus GmbH) was carried out using an excitation laser either under an angle of 65° relative to the surface normal or in a normal-incidence geometry (Fig. 2). The latter geometry is realized by an optical reflector inside the PEEM column that redirects the laser beam through the extractor lens onto the sample. This small mirror is located in the back focal plane of the objective and can be controlled very close to the axis of the electron column and allows an angle of incidence of less than 4° without influencing the image quality [7].

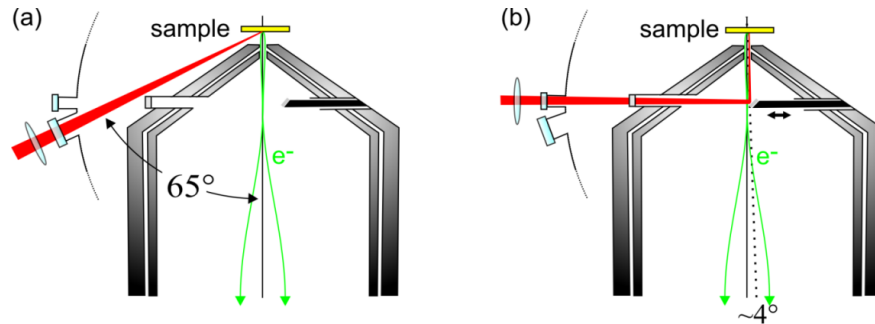


Fig. 2. Laser excitation geometries of the photoemission electron microscope. (a) Standard illumination geometry with an angle of incidence of 65° to the sample surface normal. (b) Normal-incidence excitation geometry. The light is directed to an optical mirror inside the PEEM column and illuminates the sample under an angle of $< 4^\circ$ to the surface normal. In both cases the beam is focused by a lens to a spot diameter of approximately 100 μm .

As excitation source we use 30 fs laser pulses at a repetition rate of 80 MHz with a broad spectrum in the range $\lambda = 750\text{--}850$ nm, with a peak position at 795 nm [inset Fig. 3(b)] focused down to a >100 μm diameter spot (FWHM). The corresponding photon energy (1.46-

1.65 eV) is lower than the work function of Au (4.8-5.1 eV) [8,9] and thus a multiphoton photoemission process is necessary to create photoelectrons. From the dependence of the photoelectron yield on the incident laser power (data not shown here) we conclude that the most dominant process is three-photon absorption. This high nonlinearity strongly enhances the photoemission contrast and makes PEEM very sensitive to small spatial variations of the electric field inside the material. The typical spatial resolution in detection for the PEEM technique used here is 30 nm.

Optical extinction and CL spectroscopy were used to first characterize the WGM cavity array. Individual WGM cavities were illuminated under normal incidence with the light of a broadband source through an objective lens with a numerical aperture of $NA = 0.9$. The back reflected light is detected using a spectrometer and the spectra are normalized to the signal of an unstructured area of the Au film. The resulting signal R shows a dip in the spectral range corresponding to the WGM resonance. Figure 3(a) shows the far-field extinction spectra $S = (I - R)$ for WGM cavities with radius in the range $r = 100 - 225$ nm ($d = 70$ nm, $w = 100$ nm). A clear redshift is observed for increasing cavity diameter, as expected, and the resonances are attributed to dipolar modes. Note that while these measured spectra reflect the extinction spectra, the emission spectra, while slightly different in shape, will have very similar peak resonance wavelengths.

Cathodoluminescence (CL) imaging spectroscopy was carried on the same array using a 30 keV electron beam. Light is collected using a half-paraboloid Al mirror that is placed between the electron columns and the sample, and then sent to a spectrometer [10–12]. Spectra are shown in Fig. 3(b). Again, the dipolar resonances are clearly resolved, the small additional peaks on the short-wavelength side are due to quadrupolar resonances. These weakly radiating resonances can be effectively excited using electron irradiation [13] but are not excited by a perpendicular incident optical radiation due to the mismatch of the resonant modal field pattern and the field pattern of a normal-incidence plane wave.

Photoemission results from the overlap of the excitation laser spectrum and the optical response of the excited system represented by the extinction spectrum. As can be seen in Figs. 3(a) and 3(b) this overlap systematically changes due to the spectral shift of the resonances with varying geometry. To estimate the PEEM excitation efficiency for each WGM cavity we calculate the overlap integral of the optical extinction spectrum for each WGM cavity with the laser spectrum as

$$Y_{d,r}^p = \int (S_{d,r}(\lambda) \cdot I(\lambda))^p d\lambda \quad (1)$$

where $S_{d,r}$ is the normalized optical extinction spectrum for rings with groove depth d and ring radius r . $I(\lambda)$ is the normalized spectral intensity of the laser pulse [Fig. 3(b)] and $p = 3$ reflects the order of the nonlinearity of the photoemission process. Figure 3(c) shows the resulting optical excitation efficiency map for the WGM array. As mentioned above, in the used optical extinction geometry the response is dominated by a single dipole resonance. This is represented by a characteristic intensity distribution in Fig. 3(c) forming a single streak that spans from the lower left to the upper right of the array. In an analogous manner we also calculate the overlap of the normalized CL spectra with the normalized spectral intensity of the laser pulse. Figure 3(d) shows a calculated intensity map for the array calculated using Eq. (1) for the CL data, to obtain a measure of the excitation efficiency of a PEEM experiment. Two main streaks are observed, corresponding to dipole resonances for small ring radii which are also visible in the extinction intensity map of Fig. 3(c), and an azimuthal quadrupole resonance that is observed for larger radii and smaller ring depth.

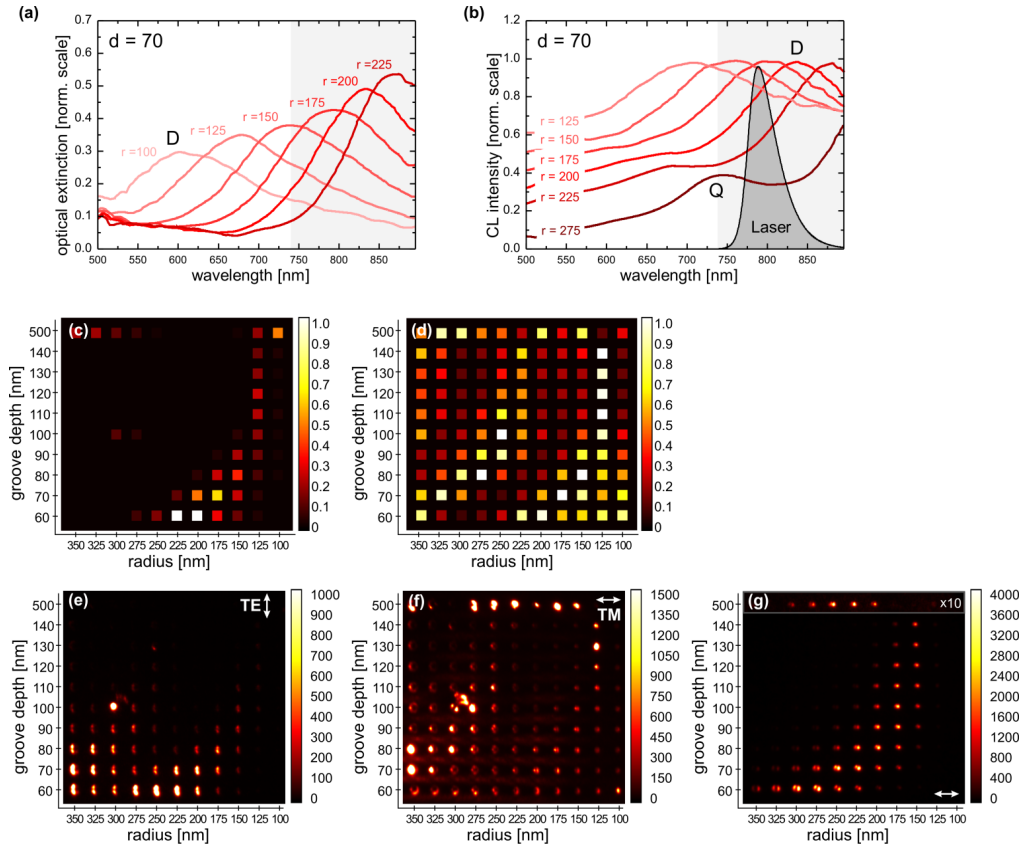


Fig. 3. (a) Optical extinction spectra of selected individual ring structures with $d = 70$ nm, $w = 100$ nm, and varying radius r , indicated in the figure. The laser spectrum used in PEEM experiments is also shown. (b) Cathodoluminescence spectra of the same rings as in (a). Calculated overlap integral $Y_{d,r}^p$ (Eq. (1)) of optical extinction (c) and CL (d) spectra with the laser spectrum used in PEEM, assuming a nonlinear process of order $p = 3$. (e-g) Experimental photoemission electron intensity micrographs of the 10×11 array of ring resonators with varying radius and depth, indicated along the axes, for oblique incidence (65° , incident from the left) with (e) TE polarized light and (f) TM polarized light, and (g) normal-incident light. The electric field components projected onto the surface are indicated by the arrows.

3. Polarization-dependent near-field imaging of dipolar modes under grazing and normal incidence illumination angle

Figures 3(e) and 3(f) show the experimental PEEM images from the array, taken with the light under an angle of incidence of 65° to the surface normal, for TE [Fig. 3(e)] and TM [Fig. 3(f)] polarized light, and under near-normal incidence [Fig. 3(g)]. In the images of Fig. 3(e) and 3(f) the light is incident from the right and the projection of the electric field vector onto the sample surface for the two polarizations is indicated by the arrows. In the case of near-normal illumination, the electric field is always in-plane, oriented as indicated in Fig. 3(g). In the case of oblique incidence [Fig. 3(e) and 3(f)], the photoemission pattern of the ring array is significantly different for TE and TM polarization. TE polarized excitation leads to a systematically enhanced photoemission from rings forming two streaks from the lower left to the upper right. One streak includes rings with small radius; the second one is shifted to rings with larger radius. Both streaks correspond well to the streaks observed in the calculated excitation image of Fig. 3(d), corresponding to dipolar and quadrupolar modes.

A very high signal-to-noise ratio is observed in the PEEM data because of the very low background yield from the flat gold surface in between the structures as the field intensity is

much lower than in the resonant grooves and the photoemission process is highly nonlinear. The PEEM image for the ring array illuminated with TM polarized laser light shows the same streaks as Fig. 3(e), but less pronounced. In contrast to TE polarized excitation the flat surface in between the structures reveals a homogeneous stripe pattern. This is attributed to the generation of surface plasmon polaritons that are excited at each structure by the out-of-plane component of the incident electric field. Normal-incidence illumination [Fig. 3(g)] leads to a single streak with a large signal-to-noise ratio, very similar to the calculated excitation spectrum of Fig. 3(c).

Next, we take advantage of the high spatial resolution of PEEM to investigate the spatial photoelectron distribution for individual resonators. Figure 4(a) shows high magnification PEEM images for the individual ring with $d = 70$ nm and $r = 300$ nm under normal incidence. Two distinctive maxima are observed along the ring circumference providing direct evidence of the dipolar nature of the resonance which is directly connected to the electric field vector of the incident light. To confirm this we changed the orientation of the electric field vector by rotating a half wave plate in the incident beam. The resulting PEEM images for four different orientations of the field vector are shown in Fig. 4. The corresponding orientation of the light vector is indicated by the arrows. As expected from the dipolar resonance the revealing electron emission pattern rotates along with the incident polarization. The slight asymmetry between the two lobes is ascribed to the off-normal incidence (4°) of the laser beam.

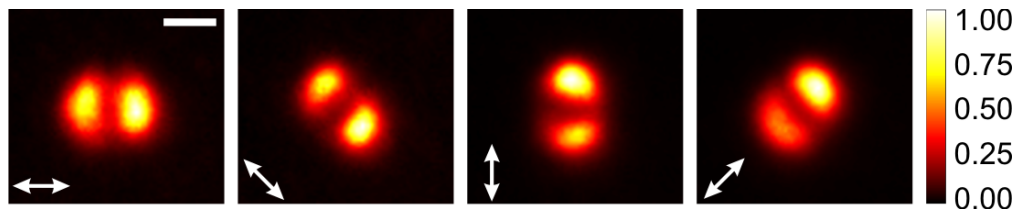


Fig. 4. High-resolution PEEM images for the dipolar resonance of a single ring resonator ($r = 300$ nm, $d = 70$ nm, $w = 100$ nm) under near normal-incidence excitation. Data are shown for four different incident polarizations (electric field direction indicated in the figure). Scale bar = 500 nm.

Figure 5 shows high-magnification PEEM images for rings with $r = 275, 300$ nm and $d = 70, 80$ nm for TM (top) and TE (bottom) polarized excitation under oblique incidence. The excitation condition with light impinging from the right to the left under an angle of incidence is sketched in Fig. 5(a). TM polarized light consists of an in-plane component parallel to the in-plane component of the wave vector of light and an out-of-plane component, while the electric field of TE polarized light is purely in-plane. For both polarizations four distinct emission maxima are observed. For TM polarization they occur at azimuthal angles of 0° , 90° , 180° and 270° , while for TE polarization, they occur at 45° , 135° , 225° , and 315° . The intensity distribution is uneven along the ring circumference in both cases: strong emission is observed at the left side (i.e. at the side away from the incident side) while only weak emission appears at the right side of the ring [14]. In contrast, no clear asymmetry is observed in the vertical direction, i.e. perpendicular to the light propagation direction.

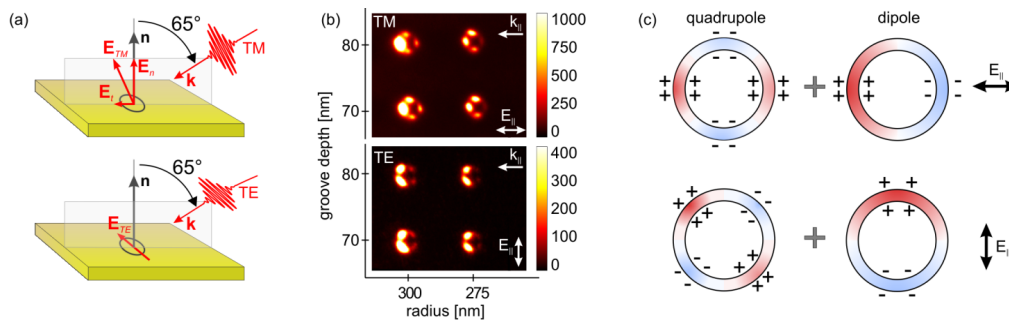


Fig. 5. High-resolution PEEM images (b) for grazing incidence for rings with $r = 275, 300$ nm and $d = 70, 80$ nm for TM (top) and TEM (bottom) polarized light whose excitation geometry is sketched in (a). The schematic (c) shows the charge distributions of quadrupolar (left) and dipolar (right) modes for TE (bottom) and TM polarization (top) whose simultaneous excitation explains the asymmetric photoelectron distribution in the PEEM images.

To analyze these distributions, Fig. 5(c) shows a schematic of the charge distribution of dipolar and quadrupolar modes in these whispering gallery resonators for TM and TE excitation. As can be inferred from the CL spectra in Fig. 3(b), the excitation wavelength of 795 nm falls right in between the dipolar (D) and quadrupolar (Q) resonance wavelengths of rings with these parameters. Thus, both resonances are excited coherently and form an asymmetric near-field distribution that is determined by the relative phase and spatial distribution of the resonant modes. The phase of each modal field distribution is directly linked to the phase of the exciting beam and the relative relation between excitation wavelength and resonance spectrum for each mode. In CL, the coherent excitation of multiple modes leads to strong angular beaming of the emission due to interference of radiation from individual modes in the far field [12]. In the present PEEM experiment, we directly derive the interference of the cavity modes from the near-field distributions recorded by the photoelectron images. Typically, the dipole resonance dominates the interaction of light with the nanostructure. Here however, as the dipole resonance is excited off-resonant and the corresponding amplitude is in the same order of magnitude as the quadrupole, the observed modulation is significant.

For TM polarization superposition of dipolar and quadrupolar modes leads to constructive interference of the resonator field at the left-hand side and to destructive interference on the right hand side [Fig. 5(c)], in agreement with the PEEM image. In contrast, by symmetry, no intensity variation is expected between top and bottom, as is observed in the experiment. For the TE polarized PEEM experiment the quadrupolar modal field distributions is rotated by 45° , compared to the TM case, in agreement with the model, as schematically indicated in Fig. 5(c). The origin of this observed change of phase between the two modes of excitation is beyond the scope of the current work. The excitation of quadrupolar resonances under oblique excitation is due to phase retardation of the incident beam across the resonator. For resonators with smaller dimensions, quadrupolar modes can still be excited, at the same wavelength, though at a smaller efficiency. For normal incidence, quadrupole excitation is forbidden by symmetry; indeed it is not observed in the experiment [Fig. 3(g)].

Figures 3(f) and 3(g) show another band of resonances for structures with the deepest grooves $d = 500$ nm when illuminated with TM polarized light. The origin of these resonances has been previously identified through CL experiments as a dipole mode in azimuthal direction ($m = 1$) of second order in radial direction ($n = 2$) [3]. This mode is strongly confined at the bottom of the groove and shows additional field maximum at the rim of the groove towards the disk in the middle. The near-field therefore contains a significant field component in the z direction. The out-of-plane component of the TM polarized light can couple to this z -component of the near-field mode, located at the disc in the middle of the ring. This induces a polarization field that furthermore couples to the groove resonance. As is confirmed by the PEEM experiment, the coupling to this mode with pure in-plane electric

field (TE polarization) is very weak and can only be observed for an excitation with TM polarized light.

4. Conclusion

We have investigated the optical resonances and modal field distributions of plasmonic whispering gallery resonators using three-photon photoelectron microscopy. The data provide direct insight into the interference of dipolar and quadrupolar modes that are coherently excited under oblique incidence at $\lambda = 795$ nm. The interference in the modal near fields is directly reflected in characteristic asymmetries in the photoelectron images for both TM and TE excitation. This work shows the power of PEEM to resolve deep-subwavelength optical field distributions and interference in photonic nanostructures, and can now be further extended in studies of a wide variety of other resonant interacting plasmonic and dielectric nanophotonic geometries.

Acknowledgments

We gratefully acknowledge discussions with Toon Coenen. This work is supported by the Deutsche Forschungsgesellschaft (DFG) within the Research Focus Program “Ultrafast Nano-Optics” (SPP 1391). The Dutch part of this work is part of the research program of the Foundation for Fundamental Research on Matter (FOM) which is financially supported by the Netherlands Organisation for Scientific Research (NWO). This research is also supported by the European Research Council. DK acknowledges funding from the Irish Research Council and the Marie Curie Actions ELEVATE fellowship.